[Supplemental Information]

Non-Thermal Plasma Upgrading of Humidified CO_2 into Syngas in a Dielectric Barrier Discharge Reactor: Tuning H_2/CO ratios via specific energy input and gas flow rate

Maxwell Klein [a], Joshua Jack [a]

[a] Department of Civil and Environmental Engineering, University of Michigan, Ann Arbor, MI, 48109, United States

*Corresponding author; Prof. Joshua Jack, Department of Civil and Environmental Engineering, University of Michigan, Ann Arbor, MI, 48109, United States (E-mail: jdjack@umich.edu)

S1.1 Reactor setup and operation

Data was taken using a BRONKHORST EL-Flow Select F-201CV-5K0 Mass Flow Controller between three separate flow rates: 1.00 $Lmin^{-1}$, 0.20 $Lmin^{-1}$, and 0.04 $Lmin^{-1}$ with H_2O concentrations of 2.4 ± 0.2 %, 2.2 ± 0.2 %, and 2.2 ± 0.2 % by gas volume. Additional details on the preparation and measurement of the humidified CO2 are provided in Section S1.2. Within these three conditions, SEI was used as the independent variable by changing the applied voltage. Since SEI is a function of power, and power is a function of voltage and current, the SEI of each test was computed retroactively. As such, SEI was dependent on the voltage and frequency of our plasma generator. Since the same SEI can produce dramatically different plasmas[14], these experiments used voltage as the sole controller of SEI for a given flow rate. The plasma generator was set to pulse at a frequency of 500 Hz with a duty cycle of 50% for all tests. Similarly, the frequency of oscillations within the pulse was maximized at a consistent value later measured to be f_{osc} = 36.5 ± 0.5 kHz across all experiments. As a result, the voltage knob of the generator was the sole controller of SEI for each experimental condition.

Given the heating of the electrode as a result of its resistance to an applied voltage, as well as the effect of heating reactor walls and gas, all experiments had to follow a strict timeline and procedure to be replicable. As such, each experiment followed a rigorous set of timed steps. All experiments took place beginning with the reactor in equilibrium with the room at a consistent 22 °C. Gas controlled by our MFC was bubbled through our humidifier for a minimum of 5 minutes to ensure that all the initial gas was flushed out and an equilibrium humidity was obtained.

Before beginning the data collection period, the gas chromatograph had to be ready for an immediate sample, and a gas bag had to be connected to the vacuum pump to minimize contamination. All items used in the procedure needed to be readily available and prepared before the data collection started. The thermal imager needed to be on and have enough storage to collect new data. Similarly, the oscilloscope software had to be collecting data over at least ten 2ms pulses and with enough resolution to sample the data many times for error estimation. The procedure sheet had to be opened and followed, and a lapping timer needed to be started to accurately track the time between major steps. Once these preparations were completed and checked against the procedure checklist, the timer was started. At the same instant the timer was

started, the CTP-2000 KP plasma generator's voltage regulator would be turned to '50V'. The frequency knob would then be delicately adjusted to the frequency that maximizes the current flowing through the system. This frequency is the *maximally efficient frequency* of the device and allows for the same frequency to be used for all experiments since it was located at the same applied voltage for each experiment. The voltage knob was then rotated until the generator displayed the preplanned voltage for the experiment. The voltage setting process consistently took between 20 – 40s; experiments that took longer were cancelled and data collection was moved to a later hour once the reactor had cooled fully.

Once the display was at the intended voltage, the timer was lapped back to 0:00 to maintain data. Precisely when seven additional minutes had elapsed, the experimenter took a thermal image of the reactor using the VEVOR Thermal IR camera. At this moment, the gas collection bag is attached to the gas outlet, and the timer is lapped again. Resistance data is immediately taken by the oscilloscope, followed by capacitance data after signal adjustments. Similarly, this collection had to take less than 45 seconds to be a usable test. Once two minutes had elapsed, a thermal image of the reactor was taken, followed by a thermal image of the gas inlet and outlets. As the picture was being taken, the gas bag was sealed, locked, and disconnected.

A 150 ± 1 μL sample was taken from our gas bag using a Hamilton Syringe within five minutes of the experiment and inserted into the front inlet of our Agilent 8890 Gas Chromatograph (GC). As soon as the gas was pumped into the inlet, the experimenter ran the gas chromatograph method. Once this had occurred, the electrode was then flushed with N_2 for a period of at least 5 minutes. Following this, the electrode was gently cleaned with Kimwipes and placed in a container lined with Kimwipes. These steps were necessary to minimize changes in the surface chemistry of the copper electrode.

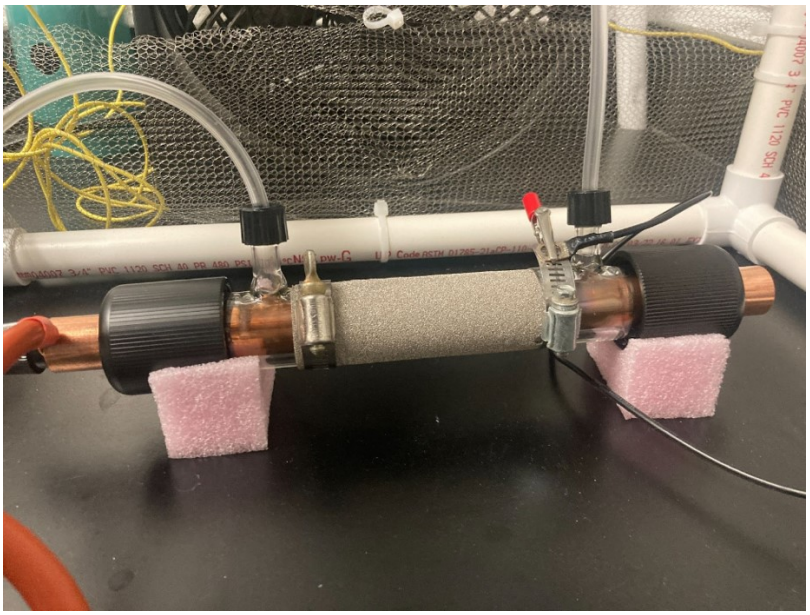

Figure S1: DBD Reactor Setup. The copper electrode runs through a sealed pyrex tube that acts as a dielectric. The inner electrode is securely connected to a plasma generator which applies a strong oscillating voltage to our reactor. A nickel foam mesh is wrapped uniformly around the tube and connected to a ground. Gas leaving the MFC (not pictured) enters into the Pyrex tube

from the left, passes through the plasma volume, and exits on the right before being collected by a gas bag. The setup is surrounded by a custom-built Faraday cage to protect electronics components from strong electric effects.

S1.2 Humidified Gas Preparation and Measurement Procedure

During each experiment, humidified CO_2 was introduced into the DBD reactor via a mass flow controller at flow rates of 1.00, 0.20, or 0.04 L min^{-1}, corresponding to residence times of 1.9, 9.6, and 48 s, respectively. The H_2O concentration was maintained between approximately 0.49 and 0.54% (v/v) across all experiments by bubbling bone-dry CO_2 through a humidification vessel containing 12 ± 2 cm of water. A 5 min equilibration period was used prior to each experiment to ensure consistent humidity at each flow rate and comparable humidity between flow conditions.

Water vapor concentration was quantified using a DwyerOmega RH-USB humidity and temperature sensor placed in a sealed enclosure downstream of the humidifier. Following the equilibration period, relative humidity was recorded for 2 min under each condition. The partial pressure of water vapor was calculated by multiplying the average relative humidity by the saturation vapor pressure of water at 25 °C (0.0313 atm). This calculation assumed that, although plasma and reactor temperatures increased during operation, the gas inlet and humidification vessel remained near ambient temperature due to thermal insulation of the tubing and water reservoir. Uncertainty was propagated quadratically.

The outlet pressure of the mass flow controller was 50 psi(g), corresponding to an absolute pressure of 4.39 atm after accounting for a 13 cm water column. This yielded water vapor partial pressures of 0.024, 0.023, and 0.022 ± 0.001 atm for flow rates of 1.00, 0.20, and 0.04 L min^{-1}, respectively, corresponding to water vapor concentrations of 0.54, 0.52, and 0.49 ± 0.02% (v/v). No measurable deviation from the set flow rates was observed during data acquisition once steady-state conditions were reached. The bone-dry CO_2 feed (99.99% purity) contained trace water vapor (< 10ppm), which was included in the overall error analysis.

Fluctuations in gas temperature and their effect on concentration were also quantified and propagated for energy efficiency calculations. Thermal images acquired at the beginning and end of the 2 min data collection period were used to estimate the average gas temperature in the reactor. These values were applied in the ideal gas law to calculate molar density, and differences between initial and final molar flow rates were used to estimate associated uncertainties.

S1.3 Gas Chromatography

The method used on our GC had to have enough resolution to measure H_2, CO, N_2, O_2, CO_2, and CH_4. This meant that our GC's method had to have a relatively low flow rate, pressure, and temperature in order to clearly separate the proximal N_2 and O_2 peaks. A clear measurement of N_2 was necessary to understand how much air had leaked into our GC column. Additionally, our experiment had to have a stable baseline reading (in μV) for any period over which a species could be measured. This meant that the temperature could not be increased to detect species with lower thermal conductivity — namely CO and CO_2 — without careful planning. After iterative

design, the final method ran at 20 $mLmin^{-1}$ at 200 °C for 4 minutes. At 4 minutes, the temperature would ramp at 75 $°Cmin^{-1}$ until it reached 135 °C, where it would remain for 4.5 minutes. This allowed for a stable reading during the periods where H_2, N_2, CO, and CO_2 were expected to appear. With this method, CH_4 was detectable at concentrations lower than 0.1% by volume, but was never observed in our output gas.

To analyze the data collected by the gas chromatograph, numerous samples of all present gases had to be obtained. Known quantities of H_2, N_2, O_2, CO, and CO_2 were used to calibrate the percentage of each species in a given sample by volume. Proper vacuuming and rapid sampling were necessary to minimize the presence of O_2 and N_2 gases that would enter the collection bag in small amounts from the surrounding air. As mentioned, since N_2 was not expected to be present in the plasma, it was used as a measurement of contamination from outside air. Nine samples ranging from 0% to 100% N_2 were used to fit the area integrated on the gas chromatograph to the N_2 concentration. O_2 was similarly calibrated. Data were then sampled directly from lab air to determine the expected ratio of O_2 to N_2 readings from pure leakage. Using this data, we were then able to calculate the percent of the total gas leaked into the bag as a function of the N_2 reading. This value was then used to scale the area reading for other species, although this never exceeded 10% and its associated error was propagated. Notably, methane (CH_4) was not detected in any condition, despite the GC's ample detection limit (<1 vol%). The absence of methane is likely due to the high activation energy required to cleave the C=O bond in CO_2 and the limited availability of H radicals from H_2O dissociation, especially under non-catalytic conditions. Therefore, high activation energies were likely unable to facilitate the production of stable CH_4 compounds. Additionally, HO_2 and H_2O_2 were assumed to be negligible.

Calibration of the other species was conducted following the N_2 calibration and enlargement procedure. The CO_2 and H_2 percentages were then compared to gas samples collected using the same procedure and experimental setup with no applied voltage to ensure consistency. Finally, these fits were then applied to the measurements conducted in each experiment to determine the percent of each species by volume and subsequently derive the molar flow rate of each species. These molar concentrations were obtained by applying the ideal gas law to the species volume concentrations and assuming that the sample accurately represented the contents of the gas bag. The flow rate was applied to these molar ratios to compute the actual flow rate of each species after plasma conversion for energy efficiency calculations.

S1.4 Electrical Analysis

In Equation 1, P represents the dissipated power in Joules per second as calculated using the technique discussed in Section 2.4, and Q represents the volumetric flow rate in liters per second. This was accomplished in python using the SciPy and NumPy packages after plotting and isolating one current wavelength within a pulse using matplotlib. Once this wavelength was precisely shifted to align with a complete cycle, it was then integrated and multiplied by the time of each step to obtain the charge [Equation 2]. To account for a slight shift due to residual applied power, the actual Lissajous figures plotted charge array minus its mean value. The dissipated powers calculated were all compared to the calculated applied powers to ensure that they were lesser, but similar in magnitude.

(1) $P_{diss} = f \oint Q_{(charge)} dV$

(2) $Q_{charge} = \sum_{0}^{\tau} Q_{(charge)} dt$

A more complicated relationship exists between SEI, flow rate, applied voltage, and pulse frequency. The primary independent variable used in this study is SEI, although SEI itself is a dependent variable of the applied voltage and current, as discussed in the methods section. Power is the product of the applied voltage and the current. Since P = IV, any specific power applied can be made from a variety of different current or voltage values. Moreover, the influence of relative humidity and pulse frequency could lead to an even larger number of possible output gases given different inputs. These variables may be altered for future studies but are held constant to develop a solid understanding of the underlying gas kinetics while changing applied voltage and flow rate.

With molar flow rates of each species, we can calculate the conversion, selectivity, and energy efficiency under each experimental condition. These molar flow rates also allowed us to easily compute the syngas ratio produced in each experiment as a function of SEI. Errors from each fitting curve were then propagated in quadrature with errors on the GC measurement, the enlargement factor, and the syringe sample volume to properly account for experimental variation.

The electrical data was sampled using an OS2202TA Digital Oscilloscope. Samples were collected at a rate of 1GS/s for roughly 10 pulses. Once this data had been calibrated to the actual voltage and current applied to the reactor, the data were then aligned in phase in *PYTHON*. Once the data were precisely aligned, power was calculated by multiplying every adjusted voltage value by its respective current value. Given the enormous size of the data, only 1 in every 1000 datapoints was sampled without losing detail on the wave shape. For an error estimate, the datasets were offset slightly and used to calculate power independently. The standard deviations were calculated and the means were used for the final SEI values. Finally, we were able to produce a Q-V Lissajous plot for each flow rate using one sample experiment. Lissajous plots become progressively wider and less well-defined with increasing SEI, a trend that is particularly clear at the lowest flow rate. This behavior is expected because the dissipated power is proportional to the area enclosed by the Lissajous figure. Accordingly, larger Lissajous areas correspond to higher dissipated power, resulting in increased SEI at a given flow rate.

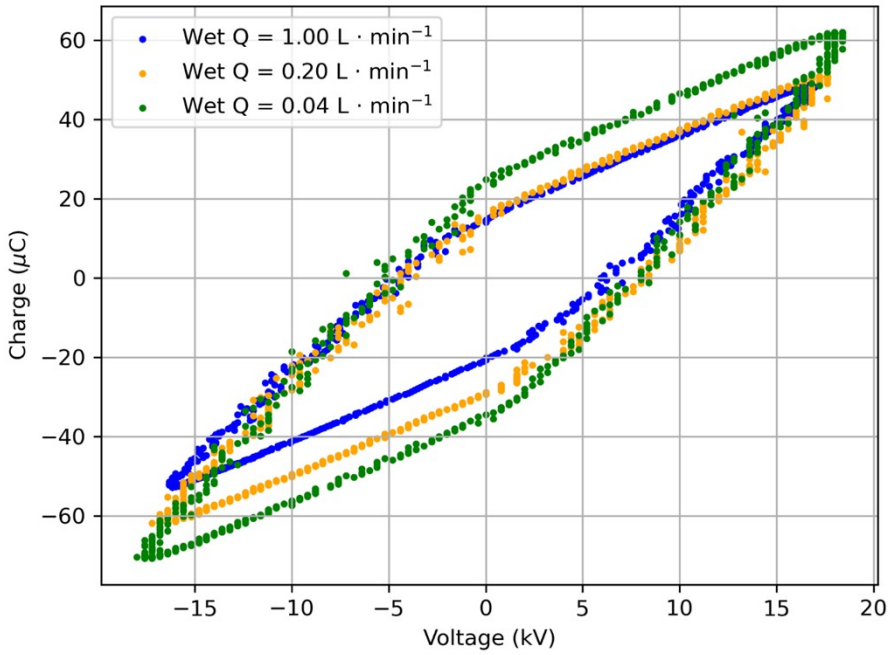

Figure S2: Representative Q–V Lissajous plots for humidified CO_2 discharges in the DBD reactor at different volumetric flow rates. Data are shown for wet CO_2 flow rates of 1.00, 0.20, and 0.04 L min^{-1}, corresponding to residence times of 1.9, 9.6, and 48 s, respectively.

S1.5 Electrical Efficiency Calculations

Energy efficiency values were calculated using Equation 3, where m represents the molar flow rates (moles per second), H is the enthalpy of molecules (eV/mol), and $P_{supplied}$ is the external power input (eV/s).

$$(3)\ \eta(\%) = \frac{m_{co}\Delta H_{CO_2} + m_{H_2}\Delta H_{H_2O}}{P_{supplied}}$$

Molar flow rates were determined by multiplying the GC-measured product mole fractions by the total outlet flow rate, as obtained from the thermal imaging analysis and mass flow controller readings. Flow-rate uncertainties were calculated by propagating the calibration uncertainty of each gas with the corresponding flow-rate error. Uncertainty in the energy efficiency was obtained by combining the uncertainty in the numerator with that of the denominator in quadrature. The supplied power was calculated using Equation S4, and its uncertainty was estimated from the variance of five time-shifted samples of the same pulse for each operating condition.

(4) $P_{supplied} = \frac{1}{\tau}\int_0^{\tau} QdV = \frac{1}{\tau}\sum_0^{\tau} QV$

The global reactions below (5, 6) were used to calculate the change in enthalpy for the formation of H_2 and CO.[13] ΔH represents the change in enthalpy from the reaction proceeding forward.

(5) $CO_2 \rightarrow CO + \frac{1}{2}O_2 \quad \Delta H = 2.9\frac{eV}{molecule}$

(6) $H_2O \rightarrow H_2 + \frac{1}{2}O_2 \quad \Delta H = 2.6\frac{eV}{molecule}$

Finally, CO_2 conversion was calculated using Equation S7, where the variables in brackets represent the molar concentration of CO_2. Errors were calculated by finding the error in the numerator and adding it in quadrature to the error in the denominator. Similarly, H_2O conversion was calculated using Equation 8, where it was assumed that the only non-negligible were H_2 and H_2O.

(7) $X_{CO_2}(\%) = \frac{[CO_2]_{input} - [CO_2]_{output}}{[CO_2]_{input}}$

(8) $X_{H_2O}(\%) = \frac{[H_2]_{output}}{[H_2O]_{input}}$

S1.6 Possible Reaction Pathway

We anticipate a reaction pathway detailed by equations (9-17), as reported by Ma et. al, 2018,[15] with rate coefficients from the zero-dimensional kinetic model in Snoeck et. al (2016). An illustrated reaction scheme with the intermediary ions, radicals, and side products can be found in Snoeck et. al (2016).

(9) $CO_2 + e^- \rightarrow CO + O + e^- -$

(10) $H_2O + e^- \rightarrow OH + H + e^- -$

(11) $CO + OH \rightarrow CO_2 + H \quad 2.8 \times 10^{-14}$

(12) $H + OH \rightarrow O + H_2 \quad 2.1 \times 10^{-16}$

(13) $H_2 + OH \rightarrow H_2O + H \quad 1.1 \times 10^{-14}$

(14) $O + O + M \rightarrow O_2 + M \quad 7.0 \times 10^{-33}$

(15) $H + O_2 + M \rightarrow HO_2 + M \quad 1.4 \times 10^{-32} - 2.9 \times 10^{-31}$

(16) $HO_2 + O \rightarrow O_2 + OH \quad 5.4 \times 10^{-11}$

(17) $H + OH + M \rightarrow H_2O + M \quad 1.5 \times 10^{-30} - 2.2 \times 10^{-29}$

It is necessary to also consider other reactions which may counteract the formation of CO or H_2 by releasing O or consuming C or H atoms.

(18) $CO + e^- \rightarrow C + O + e$

(19) $O_2 + e^- \rightarrow O + O^-$

(20) $CO + OH \rightarrow CO_2 + H$

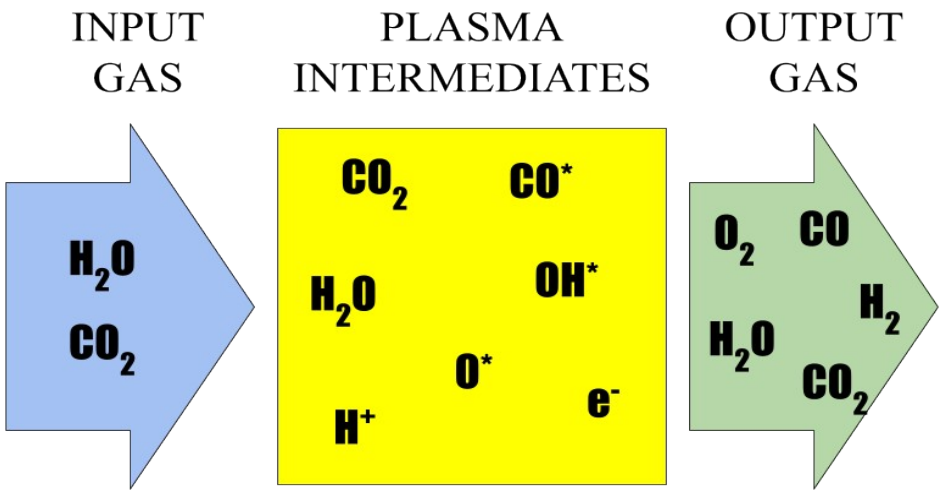

Figure S3: Potential Species Formed during NTP Syngas Production. Initially, a gas that only contains water vapor and carbon dioxide (blue arrow) is fed into the plasma reactor. When a strong oscillating voltage is applied to the gas, some of these molecules dissociate into radical species, as shown in the yellow square in the figure above. The asterisks indicate that the species has an unknown charge or arrangement of valence electrons as a result of the strong electric field.

S1. 7 Carbon Balance

A carbon balance was conducted to determine the amount of carbon deposited onto the electrode. An assumption was made, following the lack of detection of Methane in the GC, that there was no higher order carbons made in any significant concentration. Thus, we assumed that all carbon that was not directly measured as CO2 or CO was deposited onto the electrode. The results for each experiment with errors propagated in quadrature are graphed in Figure S8. With the exception of a few outliers, we see that carbon deposited steadily increases as SEI increases, owing to the higher electron temperature leading to an increase in the concentration of electrons capable of dissociating Carbon from Oxygen [Table 1].

(21) $$C_{Deposited}(\%) = \frac{[CO_2]_{input} - [CO_2]_{output} - [CO]_{output}}{[CO_2]_{input}}$$

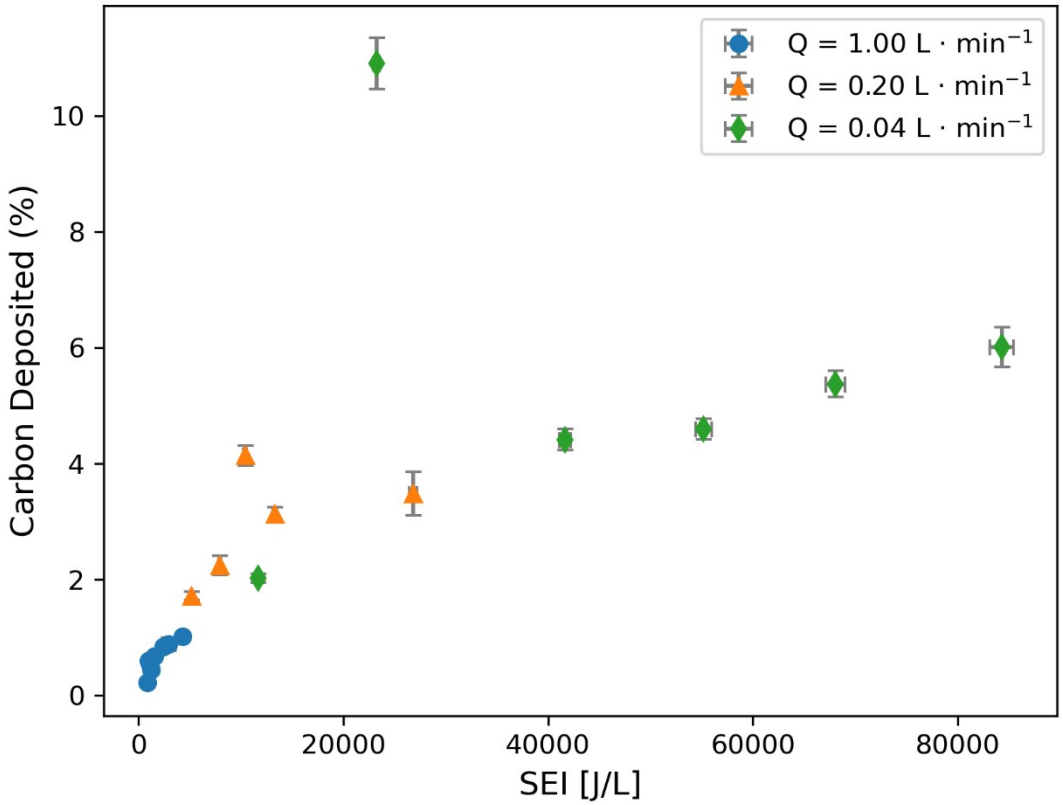

Figure S4: Carbon deposition as a function of specific energy input (SEI) at different volumetric flow rates in the DBD reactor. Data are shown for humidified CO_2 flow rates of 1.00, 0.20, and 0.04 L min^{-1}.

To calculate CO_2 conversion, we used the equation below. Errors were then propagated in quadrature.

(22) $$X_{CO_2}(\%) = \frac{[CO_2]_{input} - [CO_2]_{output}}{[CO_2]_{input}}$$

To calculate carbon deposition, we assumed that the only other significant carbon products are CO_2 and CO, as we did not detect CH_4. We computed carbon lost to deposition by subtracting the measure moles of CO_2 and CO by the initial CO_2 into the system.

(23) $$C_{Deposited}(\%) = \frac{[CO_2]_{input} - [CO_2]_{output} - [CO]_{output}}{[CO_2]_{input}}$$

The results of Figure S8 show that, with one notable exception, there is a clear positive relationship between SEI and carbon deposition. We would expect for this to occur due to the increase in electrons capable of dissociating CO at high energy levels, assuming that CO dissociation is the primary cause of soot formation [Equation 18, Figure 1f, Figure S4].

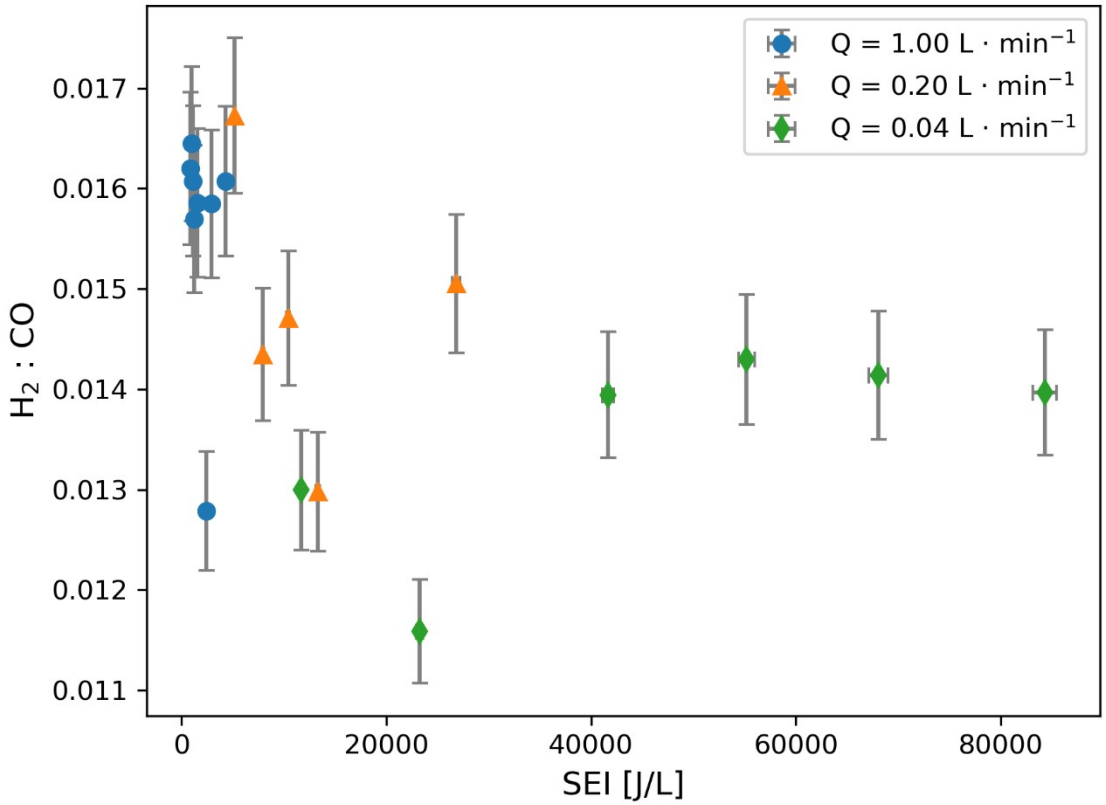

Figure S5: Dependence of syngas composition (H_2:CO ratio) on specific energy input (SEI) at different volumetric flow rates in the DBD reactor. Experiments were conducted at CO_2 flow rates of 1.00, 0.20, and 0.04 L min^{-1}, corresponding to residence times of 1.9, 9.6, and 48 s, respectively

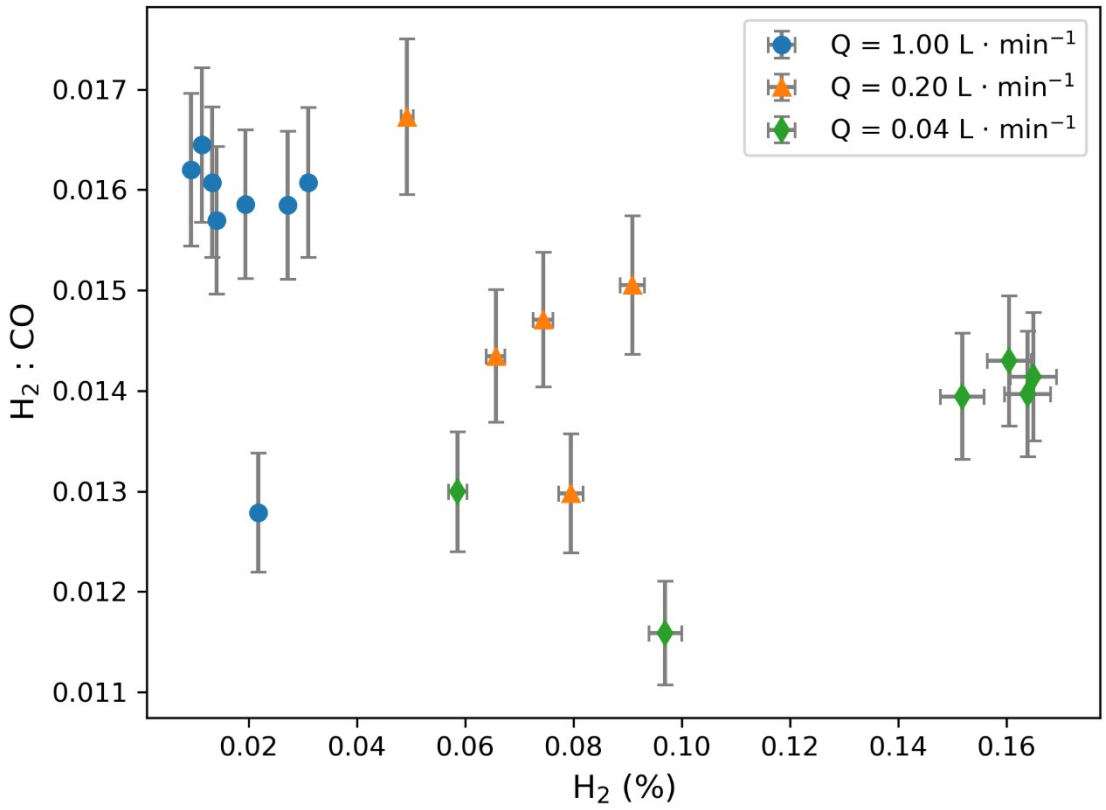

Figure S6: Relationship between syngas composition (H_2:CO ratio) and hydrogen concentration at different volumetric flow rates in the DBD reactor. Data are shown for CO_2 flow rates of 1.00, 0.20, and 0.04 L min^{-1}, corresponding to residence times of 1.9, 9.6, and 48 s, respectively.

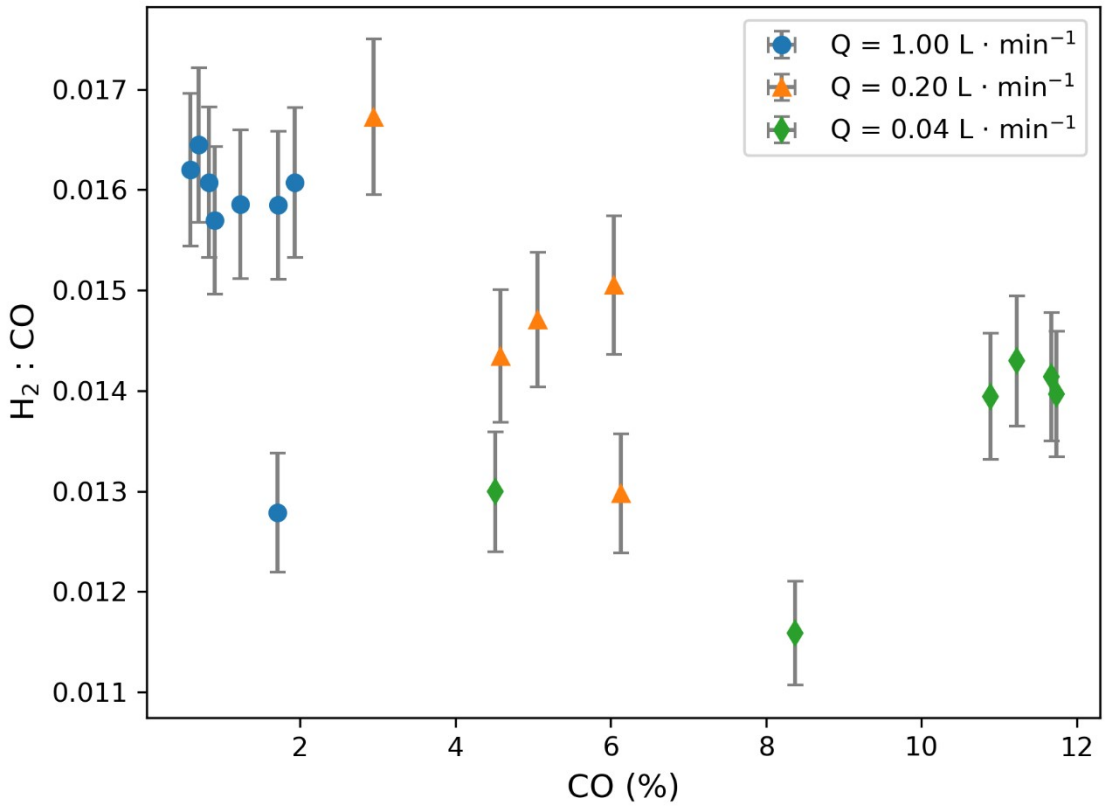

Figure S7: Impact of syngas composition (H_2:CO ratio) on carbon monoxide concentration at different volumetric flow rates in the DBD reactor. Data are shown for CO_2 flow rates of 1.00, 0.20, and 0.04 L min^{-1}, corresponding to residence times of 1.9, 9.6, and 48 s, respectively.